



Copper-alloyed spinel black oxides and tandem-structured solar absorbing layers for high-temperature concentrating solar power systems

Tae Kyoung Kim^{a,b}, Bryan VanSaders^{a,c,1}, Elizabeth Caldwell^{a,b}, Sunmi Shin^{a,b},
Zhaowei Liu^{a,c}, Sungho Jin^{a,b,*}, Renkun Chen^{a,b,*}

^a Materials Science & Engineering, University of California at San Diego, CA 92093, USA

^b Mechanical and Aerospace Engineering, University of California at San Diego, CA 92093, USA

^c Electrical & Computer Engineering, University of California at San Diego, CA 92093, USA

Received 22 November 2015; received in revised form 2 March 2016; accepted 3 March 2016

Available online 24 March 2016

Communicated by: Associate Editor Michael Epstein

Abstract

Although renewable solar power plants are rapidly proliferating, high cost and the intermittent availability of solar power are still significant barriers for its penetration into the energy grid system. Concentrating solar power (CSP) offers an attractive alternative due to its integration with cost-effective thermal energy storage systems. To further reduce the cost of CSP, it is imperative to operate the plants at higher temperatures for enhanced efficiency. One of the key components for next-generation high-temperature CSP is the solar absorbing coating materials. In this work, we have developed tandem-structured solar absorbing layers with CuFeMnO_4 and CuCr_2O_4 black oxide nanoparticles (NPs). These tandem structures exhibited a remarkably high solar-to-thermal conversion efficiency, or figure of merit (FOM), of 0.903, under the condition of 750 °C operating temperature and a solar concentration ratio of 1000. More importantly, the coating showed unprecedented durability, as demonstrated from long-term isothermal annealing at 750 °C in air as well as rapid thermal cycling between room temperature and 750 °C. Our results suggest that the tandem black oxide coating is suitable to meet the stringent demand of next-generation high-temperature CSP systems. The coating materials synthesis, structures, optical as well as thermal properties will be discussed.

© 2016 Elsevier Ltd. All rights reserved.

Keywords: Spinel black oxide nanoparticles; Solar absorbing coating; Tandem structure; Porous surface; Concentrating solar power

1. Introduction

Electricity generation is accomplished by various ways including conventional power plants based on coal, natural gas, nuclear, and hydroelectricity, as well as renewable

power plants including geothermal, biomass, wind, solar photovoltaic (PV) cells, and concentrating solar power (CSP) plants Turner, 1999; Varun et al., 2009; Khamwannah et al., 2012; Ho and Iverson, 2014; Hayman et al., 2008. In 2012, electricity generation from the renewable sources in US amounted to ~13% and it is anticipated to grow up to 18% in 2040 according to the projection of US Energy Information Administration (EIA) [Levelized Cost and Avoided Cost of New Generation Resources, 2014](#). When estimating levelized

* Corresponding authors at: Materials Science & Engineering, University of California at San Diego, CA 92093, USA.

E-mail addresses: jin@ucsd.edu (S. Jin), rkchen@ucsd.edu (R. Chen).

¹ Present address: University of Michigan, Ann Arbor, MI 48109, USA.

cost of electricity (LCOE) in 2019, solar thermal electricity generation such as concentrating solar power (CSP) systems will still be around 3 times higher in LCOE than nuclear power plant and wind power plant (Levelized Cost and Avoided Cost of New Generation Resources, 2014). To make CSP cost effective, US Department of Energy (DOE) targets to reduce the LCOE of CSP to 6 ¢/kWh by 2020 which is ~30% of the LCOE in 2010 (21 ¢/kWh) (Tackling Challenges in Solar, 2014). To reach this target, it is necessary to develop advanced materials and structures to improve the performance and reduce the cost of CSP systems. Among various components of a CSP system, the solar absorber is a critically important element. Solar absorbers are typically made of metallic alloy tubes, inside which heat transfer fluids (HTFs) are heated up by the absorbed solar energy to generate high-pressure steam for power generation (Burhardt et al., 2011; Moon et al., 2014). To enhance the solar absorbing capability, the tubes are usually coated with spectrally selective coating layers (for parabolic trough systems) or solar absorbing layers (for solar towers) (Burhardt et al., 2011; Moon et al., 2014; Behar et al., 2013). To reach the DOE target, the following conditions on solar absorbers have to be achieved: HTF exit temperature ≥ 650 °C, solar to thermal efficiency $\geq 90\%$, and lifetime $\geq 10,000$ cycles (Tackling Challenges in Solar, 2014). However, solar absorber temperature of today's tower type CSP plant is around 550 °C. As the efficiency of Carnot cycle type thermal device can be substantially increased by higher temperature operation, it is highly desirable to obtain a new solar absorber coating material that can withstand higher temperature exposure (such as 750 °C or higher) with long-term stability of structures and optical and thermal behavior.

Conventional solar receivers in solar tower plants are coated with a commercially available black paint named Pyromark. Pyromark-coated samples on Inconel 625 substrates showed degradation after 300 h isothermal annealing at 750 °C in air, as reported by Sandia National Laboratories (Ho et al., 2014). In order to increase the FOM, multi-layered solar absorbing layers have been developed using metal thin films with low IR emission (Kennedy, 2002). However, this type of tandem structure with metal films can only be used in vacuum or under inert environment as in parabolic troughs, and is not suitable for high-temperature solar towers because it can be easily oxidized in air.

The scientific and engineering challenges of achieving simultaneous high solar absorptivity and high temperature durability lie in the difficulty of ensuring stability of structures and optical properties of metallic, ceramic or carbon based absorber materials at high operating temperatures (e.g. 750 °C or higher) in air. Sturdy structures with nanoscale features can promote light trapping, diffuse and react optically well below their bulk melting point. Furthermore, multilayer thin film structures are prohibitively expensive to deposit on large surface area (hundreds of square meters

per solar tower) in solar thermal plant structures. Also, the use of exotic nanopatterning for improved light absorption or the use of nanophotonic structures will be too costly for solar thermal plant applications.

In this work, we overcome these challenges by adopting a number of novel strategies to demonstrate a new black oxide nanoparticle structure that is easy to produce by a simple spray coating process, exhibiting superior thermal stability and optical performance at high temperature. First, we synthesized spinel type (AB_2O_4) copper-alloyed black oxide nanoparticles. Spinel metal oxides have been attractive to thermal applications because of their oxygen stoichiometry and crystal structure stability at high temperature (Ambrosini et al., 2011; Vince et al., 2003; Bayon et al., 2008). Second, we utilized a two-layer tandem structure, consisting of a top layer of Cu–Fe–Mn oxide for absorption in the visible and near-infrared (IR) spectrum and a bottom layer of Cu–Cr oxide responsible for near-IR absorption. Finally, we employed a highly scalable spray coating technique that created porous surfaces for efficient light trapping (Moon et al., 2014; Peng et al., 2005; Tsakalakos et al., 2007; Zhu and Cui, 2010; Kelzenberg et al., 2010). By combining these novel features, as shown schematically in Fig. 1(a), our two-layered black oxide samples exhibited a high FOM and high-temperature durability.

2. Materials and methods

2.1. Synthesis of spinel Cu-alloyed metal oxide nanoparticles

Two types of black oxide nanoparticles with spinel structure were synthesized hydrothermally utilizing the co-precipitation method modified from what was reported in our prior publication (Kargar et al., 2015). For the synthesis of copper chromates, 1 M of copper chloride ($CuCl_2 \cdot 2H_2O$) aqueous solution was mixed uniformly with 1 M of chromium chloride ($CrCl_3 \cdot 6H_2O$) aqueous solution with vigorous stirring for 5 h, followed by co-precipitation into Cu–Cr hydroxides by addition of 10 M NaOH into the solution. After mixing the co-precipitated hydroxides for 2 h, hydrothermal synthesis was carried out in a 45 mL autoclave with a Teflon liner at 200 °C for 20 h. During the post-treatment, centrifuged particles were dried with a freeze-dryer and finally crystallized at 550 °C for 5 h or 750 °C for 2 h in air. With this procedure, copper chromates with two different compositions were synthesized, namely 1:1 and 1:2 in atomic ratio of Cu/Cr.

In the case of the spinel Cu–Fe–Mn oxide, the overall synthesis procedure was the same as that of copper chromates, except that the precursor solutions were made of the mixture of 1 M copper chromite ($CuCl_2 \cdot 2H_2O$), 1 M iron chloride ($FeCl_3 \cdot 6H_2O$) and 1 M manganese chloride ($MnCl_2 \cdot 4H_2O$) aqueous solution with different volumes depending on the atomic stoichiometry of Cu–Fe–Mn oxides. Cu–Fe–Mn nanoparticles with different compositions were synthesized, including 1:1:1, 0.5:0.5:2.0,

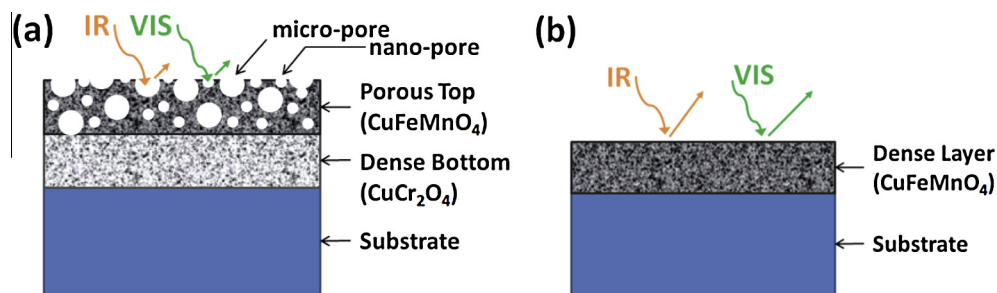


Fig. 1. Concept diagrams showing the layer structure and its effect on optical reflectance of (a) the tandem-structured solar absorbing layer with a porous top layer coated on a dense bottom layer and (b) the single-layered solar absorbing sample with a dense layer. (IR: infrared spectrum, VIS: visible spectrum).

1.125:0.75:1.125, 2.0:0.5:0.5, and 0.5:2.0:0.5 in atomic ratio of Cu/Fe/Mn.

2.2. Fabrication of tandem-structured solar absorbing layers

Using the synthesized Cu–Fe–Mn oxide and copper chromate nanoparticles, solar absorbing layers were fabricated with the following procedure. Resin (binder) solution of 7 wt% was made of methyl phenyl polysiloxane solution (SILIKOPHEN P80/X, Evonik) diluted with additional solvents (isobutanol, and xylene). In the case of dense layers, black oxide particles were dispersed in the binder solution with a weight ratio of 1/0.25 (particles/resin) through slow ball milling for 24 h, and then the mixed solution was spray-coated onto Inconel 625 substrates. The coated samples were dried at room temperature for one day, followed by curing and annealing via multi-step heat treatments in air: room temperature –100 °C for 10 min, 250 °C for 2 h, 550 °C for 3 h, 750 °C for 2 h, and finally back to room temperature. Samples with 25 μm thick coating layers could be obtained from these processes. The maximum annealing temperature (750 °C) was determined based on the target operation temperature of the solar absorber. Particle growth during the annealing process is expected to be suppressed due to the presence of the matrix material (spin-on glass).

To make the porous layers, we followed our prior approach of using sacrificial polymer beads (Moon et al., 2015). In this process, both the black oxide nanoparticles and polymer beads (Soken Chemical & Engineering) were dispersed into the binder solution with a weight ratio of 1.0/0.8/1.1 (particles/beads/binder resin) using a probe-type sonicator. We used two types of polymer beads, namely, cross-linked polystyrene beads with nominal size of 1.3 μm (SX-130H) and acrylic beads of 400 nm (MP2701). The coating procedure for making the porous layer is identical as that for the dense layer. The porous coating layer with ~5 μm thickness could be fabricated on top of the dense coating layer to make 2-layered tandem structure or on the bare substrate of Inconel 625 as a single coating layer. Especially, two-layer solar absorbing samples fabricated with a porous top layer of CuFeMnO₄

particles and a dense bottom layer of CuCr₂O₄ particles will be named CuFeMnO₄(PT)/CuCr₂O₄(DB).

Fig. 1(a) shows a schematic illustration of a 2-layered tandem structure fabricated from a porous top layer of CuFeMnO₄ nanoparticles and a dense bottom layer of CuCr₂O₄ nanoparticles. During the multi-step heat-treatment from room temperature (RT) to 750 °C following the spray-coating, the polymer beads were decomposed, after which micro- and nano-pores are expected to form, as shown schematically in Fig. 1(a).

For comparison, we also obtained Pyromark 2500 black paint (LA-CO) which is the state-of-the-art coating material for CSP solar towers. The Pyromark paint was diluted with additional solvents (xylene, and toluene), followed by the identical spray-coating, curing and annealing processes used for our black oxide samples.

2.3. X-ray diffraction (XRD) analysis

We carried out X-ray diffraction (XRD) analysis to investigate the crystal structure of copper iron manganese oxide (CuFeMnO₄) NPs, and copper chromate (CuCr₂O₄) NPs. Crystal structures of the synthesized materials were characterized using a Bruker D2 Phaser XRD with Cu K_α (λ = 0.154 nm) as the radiation source. The scanning of 2θ angle (degree) was made in the range of 10°–80° with a scanning rate of ~0.0406 deg/step and 1 step/s.

2.4. Scanning electron microscopy (SEM) and Focused Ion Beam (FIB)

SEM (Oxford, acceleration voltage of 10 kV) was used to image the shapes of CuFeMnO₄ and CuCr₂O₄ NPs, and the morphology of the top surface of the black oxide samples. For cross-sectional imaging, FIB (Scios™, FEI Company) sectioning was employed prior to SEM imaging.

2.5. Visible/infrared (IR) reflectance measurement system

An integration sphere (4" LabSphere®, Spectrafect® coated) was assembled with an Andor® Shamrock 303i spectrometer which was equipped with Si and

InGaAs-based detectors for visible/IR reflectance measurement. An incidence angle of 12.5° was applied to measure the optical reflectance of prepared solar absorbing samples in the spectral range of 300–2000 nm at room temperature. The integration sphere was used to collect all angles of reflectance.

2.6. Figure of merit (FOM)

The figure of merit (FOM) value was evaluated with the measured reflectance data to compare the conversion efficiency of solar to thermal energy of solar absorbing layers used for solar receivers, and is defined as (Moon et al., 2015):

$$\text{FOM} = \frac{\int_0^\infty (1 - R(\lambda))I(\lambda)d\lambda - \frac{1}{C} \left[\int_0^\infty (1 - R(\lambda))B(\lambda, T)d\lambda \right]}{\int_0^\infty I(\lambda)d\lambda} \quad (1)$$

where $R(\lambda)$ is the spectral reflectivity, $I(\lambda)$ is the spectral solar irradiance per unit area as defined by the reference solar spectral irradiation (ASTM G173), $B(\lambda, T)$ is the spectral thermal emissive power of a black body at temperature T , and C is the solar concentration ratio. In this work, the FOM values were calculated by assuming $T = 750^\circ\text{C}$ and $C = 1000$ which are the conditions of high-temperature CSP plants. We also used wavelength ranging from 300 nm to 20 μm to calculate the FOM value and the reflectance measured at 2 μm is extrapolated to be the reflectance in the IR spectrum from 2 to 20 μm . For systems with a large solar concentration ratio C , such as solar towers that typically have C 's greater than 1000, the optical absorption (related to optical reflectance properties) within the solar spectrum the overwhelmingly dominates the FOM values, so it is reasonable to extrapolate the reflectance data beyond 2 μm .

2.7. Thermal endurance evaluation

Thermal endurance of the fabricated black oxide layers was evaluated with thermal tests in air. Isothermal tests at 750°C in air for 500 h were carried out for the tandem-structured samples of $\text{CuFeMnO}_4(\text{PT})/\text{CuCr}_2\text{O}_4(\text{DB})$. Additionally, 100 cycles of rapid thermal cycling from RT to 750°C were carried out with a temperature ramping rate of $\pm 150^\circ\text{C}/\text{min}$ on the black oxide samples as well as the Pyromark samples. FOM endurance was evaluated with following equations after the thermal annealing and cycling tests:

$$\begin{aligned} &\text{Isothermal FOM endurance} \\ &= \frac{\text{FOM}(t = 500 \text{ h}; 750^\circ\text{C})}{\text{FOM}(t = 0 \text{ h}; 750^\circ\text{C})} \end{aligned} \quad (2)$$

$$\begin{aligned} &\text{Thermal cycling FOM endurance} \\ &= \frac{\text{FOM}(n = 100; 25 \text{ to } 750^\circ\text{C})}{\text{FOM}(n = 1; 25 \text{ to } 750^\circ\text{C})} \end{aligned} \quad (3)$$

3. Results and discussion

3.1. Materials characterization

The crystal structures of Cu-alloyed black oxide nanoparticles are analyzed with XRD as shown in Fig. 2. As-prepared CuCr_2O_4 particles have a main plane (211) at $2\theta = 35.19^\circ$ and have a tetragonal crystal system with body-centered lattice (Crottaz et al., 1997; Chukalkin et al., 1985). After the rapid thermal cycling (RT- $750^\circ\text{C}/100$ cycles) and isothermal annealing ($750^\circ\text{C}/500$ h) in air, the particles retain the original CuCr_2O_4 crystal structure and their particle size increases due to the sintering at high temperature, as illustrated in Fig. 2(a). Based on this XRD analysis, CuCr_2O_4 nanoparticles are thermally stable at 750°C in air because there is no obvious new phase appearing after the thermal tests. Similarly, crystal structures of CuFeMnO_4 are confirmed by XRD analysis, as shown in Fig. 2(b). As-prepared CuFeMnO_4 particles have a main plane (311) at $2\theta = 35.6^\circ$ and are made of a cubic crystal system with a space group of Fd-3m, which matches well with the reported XRD data (Jogalekar, 1967). These CuFeMnO_4 nanoparticles are also proved to be stable at 750°C in air after the same thermal tests as to CuCr_2O_4 nanoparticles.

3.2. Optimization of atomic composition and crystallization temperature

As mentioned earlier, we have synthesized two types of copper chromate nanoparticles with atomic ratios of 1:1 and 1:2 between Cu and Cr, respectively. Each type of the materials is subsequently crystallized at 550°C for 5 h or 750°C for 2 h, both in air, as the final step of the synthesis. Fig. 3 shows the SEM images of the copper chromates synthesized under these four different conditions. Copper chromates crystallized at 550°C possess particles smaller than 50 nm, for both 1:1 and 1:2 Cu/Cr ratios. When crystallized at 750°C , copper chromate with 1:1 Cu/Cr ratio has particle sizes ranging from 200 to 600 nm (Fig. 3(b)), whereas that with 1:2 Cu/Cr ratio grows to larger sizes (300 nm–1 μm), as shown in Fig. 3(d). Fig. 3(e) shows the spectral reflectance and FOM values of dense coating samples fabricated with the four different copper chromate particles. The figure shows that CuCr particles with a higher Cr content and lower crystallization temperature (550°C) possess the lower reflectance and the higher FOM value (0.892). Therefore, CuCr_2O_4 crystallized at 550°C is selected for further processing into the tandem structure. Our results are consistent with prior observations that CuCr_2O_4 has lower reflectance in the visible and NIR range compared to CuCrO_4 (Liang et al., 2005; Kocsis et al., 2013) and the lower crystallization temperature leads to smaller Cu chromate particles (Yuan et al., 2014).

Similar composition and crystallization temperature optimizations are applied to Cu–Fe–Mn oxide particles. Based on our results from the copper chromates, we kept

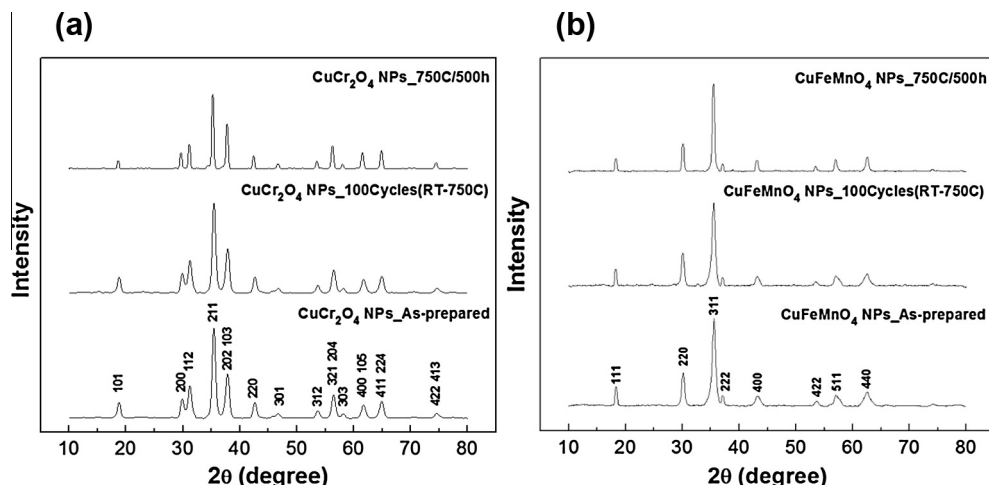


Fig. 2. XRD analysis for (a) synthesized CuCr_2O_4 nanoparticles and (b) CuFeMnO_4 nanoparticles in as-prepared state, after thermal cycling (RT-750 °C/100 cycles) in air, and after isothermal annealing at 750 °C for 500 h under air.

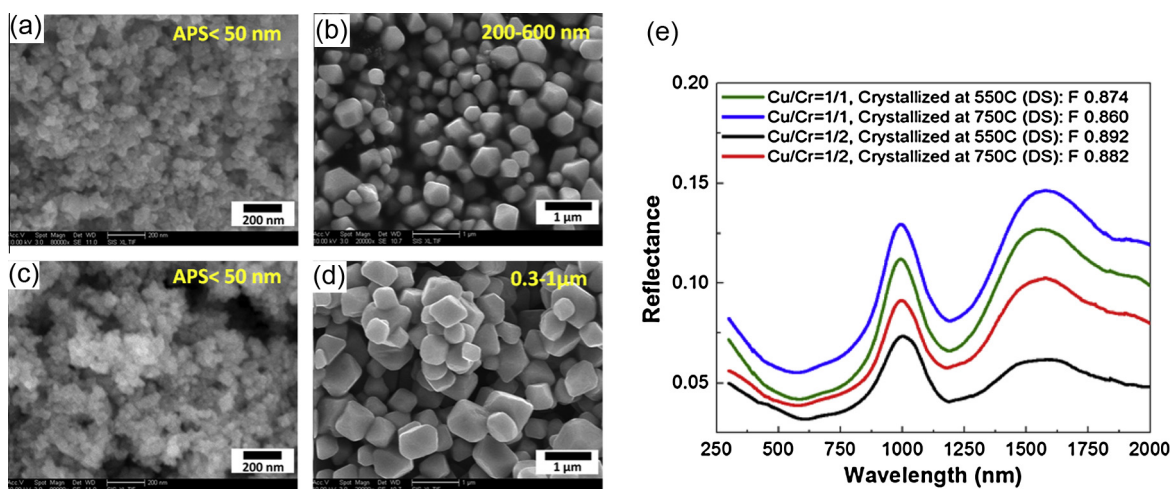


Fig. 3. SEM images and reflectance measurement results of copper chromate nanoparticles synthesized with different conditions of atomic ratio of Cu/Cr and crystallizing temperature; (a) 1/1, and 550 °C/5 h/air, (b) 1/1, and 750 °C/2 h/air, (c) 1/2, 550 °C/5 h/air, and (d) 1/2, 750 °C/2 h/air. (DS: a dense single layer coated without using pore-forming polymer beads).

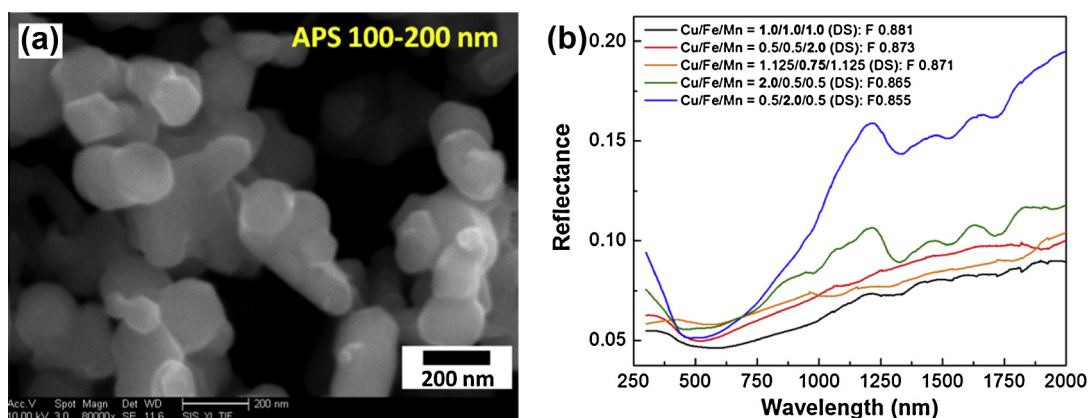


Fig. 4. (a) SEM images of CuFeMnO_4 nanoparticles crystallized at 550 °C/5 h, and (b) reflectance measurements of solar absorbing layers with a dense single layer composed of Cu–Fe–Mn oxide nanoparticles having different atomic compositions.

the crystallization temperature constant at 550 °C for Cu–Fe–Mn oxides. This temperature resulted in similar particle size of 100–200 nm (Fig. 4(a)) for different compositions. We then optimized the material composition, namely, Cu/Fe/Mn atomic ratios. The main reasoning why we adjusted the relative amount of Fe and Mn atoms is to effectively control the spectral reflectance. We have chosen the Cu–Fe–Mn oxides due to its strong absorption in the visible and near-IR spectrum. Fig. 4(b) shows reflectance data and FOM values of dense coating layers made of Cu–Fe–Mn oxide nanoparticles having five different atomic compositions of Cu/Fe/Mn, among which Cu/Fe/Mn = 1/1/1 exhibits the highest FOM (0.881). From this experiment, some useful trends can be obtained with regard to optical properties change of coating layers with atomic compositions: in Cu–Fe–Mn oxides, a larger amount of Fe (e.g., Cu/Fe/Mn = 0.5/2.0/0.5) increases the reflectance in the NIR spectrum (>750 nm), and a larger amount of Cu (e.g., Cu/Fe/Mn = 2.0/0.5/0.5) increases the reflectance in the visible and NIR spectrum, whereas a larger amount of Mn (e.g., Cu/Fe/Mn = 0.5/0.5/2.0) only slightly increases the reflectance compared to the optimal composition of 1/1/1.

3.3. Tandem-structured solar absorbing layers with a porous top layer

Having identified the optimal compositions and crystallization temperatures (e.g., CuCr_2O_4 and CuFeMnO_4 , both crystallized at 550 °C), we seek to further reduce the reflectance in the solar spectrum. First, using synthesized CuFeMnO_4 nanoparticles, we introduce porous layers

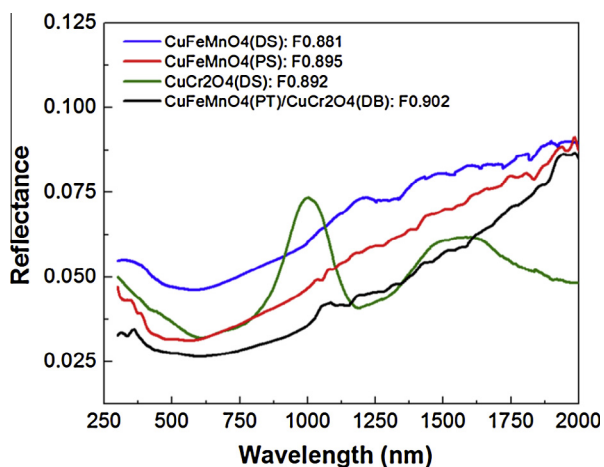


Fig. 5. Reflectance and FOM comparison amongst different solar absorbing layers. A dense single layer of CuFeMnO_4 NPs (blue line), a porous single layer of CuFeMnO_4 NPs (red line), a dense single layer of CuCr_2O_4 (green line), and two-layered tandem structure with a porous CuFeMnO_4 top layer and a dense CuCr_2O_4 bottom layer (black line). (DS: a dense single layer, PS: a porous single layer, PT: a porous top layer, and DB: a dense bottom layer). (For interpretation of the references to colour in this figure legend, the reader is referred to the web version of this article.)

(Fig. S1(b)) by using sacrificial polymer beads as described in the experimental section. Fig. 5 shows that a porous layer of CuFeMnO_4 particles has lower reflectance than a dense layer of CuFeMnO_4 particles. Second, by comparing the spectral reflectance data of CuCr_2O_4 (DS) and CuFeMnO_4 (DS) shown in Fig. 5, one can see that the CuCr_2O_4 exhibits a peak in the reflectance at around 1 μm , while CuFeMnO_4 shows an increasing reflectance above $\sim 1.1 \mu\text{m}$. Therefore, by making tandem structures that combine the light absorption capabilities of both materials, one can anticipate a lower overall reflectance. Indeed, tandem structures with a porous top layer of CuFeMnO_4 (PT) and a dense bottom layer of CuCr_2O_4 (DB) possess a low reflectance across the wide spectrum from 300 nm to $\sim 1.6 \mu\text{m}$, leading to the highest FOM value (0.902) amongst all the samples.

The higher FOM in the tandem structure can be a result of three effects: (i) combined light absorbing capabilities of CuCr_2O_4 and CuFeMnO_4 , as discussed above; (ii) the gradation of refractive index and light trapping caused by the porous top and dense bottom structures; (iii) larger overall thickness (5 μm PT and 25 μm DB layers in the tandem structure vs. 5 μm porous or 25 μm dense single layers). It is plausible that the graded refractive index could help lower the reflectance further. The top CFM layer with the porous structure has an effective refractive index closer to that of air, which leads to the reflection from the surface as well as light trapping effect by increasing the light path, and also the tandem structure induced a gradual change in the refractive index from the air to the Inconel substrate. Consequently, our tandem structure with a porous top layer yields a reduction in the Fresnel reflection over the broad spectral range (up to $\sim 2 \mu\text{m}$). Fig. 5 also suggests that the bottom CuCr_2O_4 layer in the tandem structure also contributes to the light absorption within almost the entire spectral range, i.e., from $\sim 300 \text{ nm}$ to $\sim 1.6 \mu\text{m}$, thereby reducing the reflectance of the porous single (PS) layer (red curve). This suggests that the top 5 μm PT CFM layer is perhaps not optically thick within this spectral range. However, we can ensure that the bottom 25 μm -thick CuCr layer is optically thick, based on its optical absorption coefficient ($\alpha = 100 - 300 \text{ mm}^{-1}$ or penetration depth $\sim 10 - 30 \mu\text{m}$ Levinson et al., 2005). Therefore, the lowered reflectance at the wavelengths ($< 1.6 \mu\text{m}$) originates from the combined light capabilities of two materials, rather than the increased thickness since the 25 μm -thick bottom layer is already optically thick. Above 1.6 μm , the tandem structure shows a higher reflectance than the single layers made of CuCr_2O_4 and does not follow the ultralow reflectance of the bottom CuCr_2O_4 layer. This suggests that the 5 μm -thick PT CFM layer is already optically thick, and the reflectance is likely caused at the air/CFM interface, presumably because the light trapping in the porous structure is not as effective at long wavelength.

Fig. 6 depicts the cross-sectional images observed with the FIB-assisted SEM analysis, showing that a porous

layer of CuFeMnO_4 particles with $\sim 5 \mu\text{m}$ thickness is coated on a dense bottom layer. The porous top layer consists of micro-pores ($1\text{--}2 \mu\text{m}$) and nano-pores ($100\text{--}500 \text{ nm}$), as expected from the design shown in Fig. 1(a) and the sizes of polymer beads ($1.3 \mu\text{m}$ and 400 nm). The bottom layer of CuCr_2O_4 particles contains only nano-pores formed during solvent evaporation, as shown in the right images of Fig. 6. For comparison, the left images in Fig. 6, obtained from a sample consisting of a single dense layer of CuFeMnO_4 particles and shows that there are nano-pores throughout the entire layer thickness. And also the effectiveness of the tandem structure is further demonstrated by the lower FOM values observed in single porous layers made of mixture of CuFeMnO_4 and CuCr_2O_4 nanoparticles (Fig. S2).

3.4. FOM endurance by isothermal and thermal cycling tests

After annealing the sample at $750 \text{ }^\circ\text{C}$ in air for 500 h, the $\text{CuFeMnO}_4(\text{PT})/\text{CuCr}_2\text{O}_4(\text{DB})$ sample shows a slight increase in the reflectance within a wide spectrum including visible and near-IR (Fig. 7(a)). The porous surface morphology with nano-scaled pores and micro-scaled pores can be degraded at high temperature ($750 \text{ }^\circ\text{C}$) for 500 h, which can result in the increase of reflectance in wide spectrum. In $\text{CuFeMnO}_4(\text{PT})/\text{CuCr}_2\text{O}_4(\text{DB})$ sample, $1 \mu\text{m}$ peak emerged after isothermal annealing at $750 \text{ }^\circ\text{C}$. Apart from the degradation of porous structure, another possible reason for this new $1 \mu\text{m}$ reflectance peak may result from the new phase formation of CuO after a long time

annealing at high temperature, because the coating layer made of CuO NPs (purchased from Sigma–Aldrich, US) increases reflectance in near-IR spectrum from 800 nm wavelength, as shown in Fig. S3. The fundamental reason of $1 \mu\text{m}$ reflectance peak has to be studied in future research. $\text{CuFeMnO}_4(\text{PT})/\text{CuCr}_2\text{O}_4(\text{DB})$ sample has FOM value of 0.903 in as-prepared state which is regarded as the best conversion efficiency of solar to thermal energy yet achieved for these conditions (temperature = $750 \text{ }^\circ\text{C}$, $C = 1000$, air) and it resists degradation (FOM of 0.896) from thermal testing ($750 \text{ }^\circ\text{C}$ for 500 h under air environment). After the isothermal test, this tandem-structured solar absorbing samples show an FOM endurance of 0.992 which can be evaluated with Eq. (2). After the isothermal annealing at $750 \text{ }^\circ\text{C}/500 \text{ h}/\text{air}$, the porous surface morphology is seen to be preserved except for moderate particle growth (Fig. 8(a-1) and (a-2)). Particle and crystal growth can reduce the degree of multi-scaled surface morphology, which will increase reflectance and lower the FOM values.

In rapid thermal cycling tests (RT- $750 \text{ }^\circ\text{C}/100$ cycles), Fig. 7(b) shows both $\text{CuFeMnO}_4(\text{PT})/\text{CuCr}_2\text{O}_4(\text{DB})$ sample and Pyromark sample has similar behaviors in that reflectance increases in visible spectrum and decreases in near-IR spectrum longer than $1 \mu\text{m}$ after thermal testing. The reflectance increase in the visible portion of the spectrum can be explained by the reduction of surface nano-pores by high temperature particle growth and sintering. However, dominant factors affecting the reflectance decrease in near-IR above $1 \mu\text{m}$ have to be studied in more

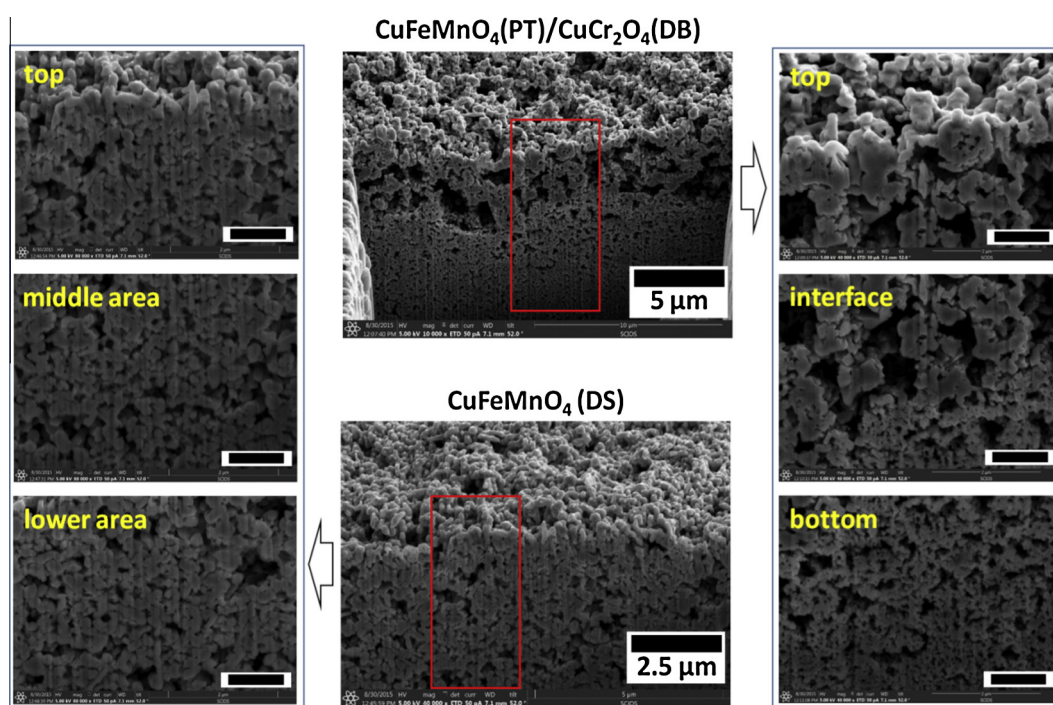


Fig. 6. Cross-sectional SEM images assisted with FIB slicing for 2-layered tandem structure of $\text{CuFeMnO}_4(\text{PT})/\text{CuCr}_2\text{O}_4(\text{DB})$ sample and a dense single-layered CuFeMnO_4 sample. In red rectangular areas, the zoomed-in images were observed from top to lower space. (Black scale bars: $1.0 \mu\text{m}$). (For interpretation of the references to colour in this figure legend, the reader is referred to the web version of this article.)

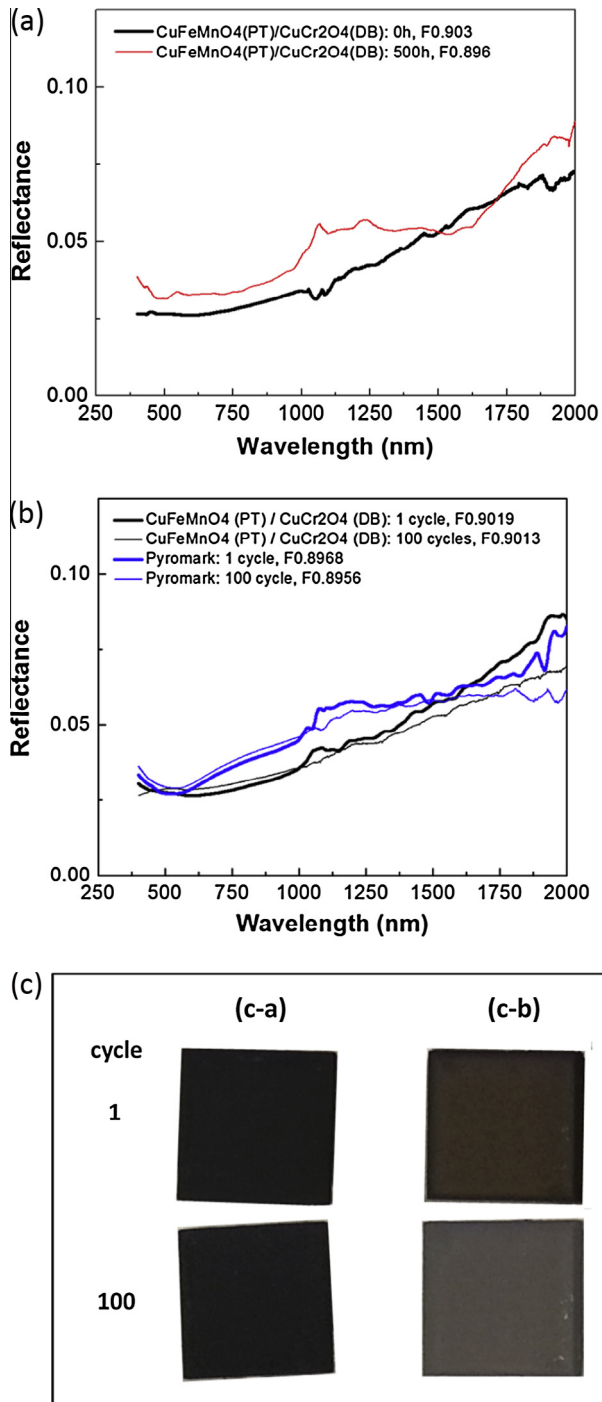


Fig. 7. Reflectance measured from (a) isothermal tests (750 °C/500 h) for $\text{CuFeMnO}_4(\text{PT})/\text{CuCr}_2\text{O}_4(\text{DB})$ sample, and (b) thermal cycling test (RT-750 °C/100 cycles) for $\text{CuFeMnO}_4(\text{PT})/\text{CuCr}_2\text{O}_4(\text{DB})$ sample and lab-coated Pyromark sample, and (c) photo images taken from thermal cycling tests after 1 cycle and 100 cycles; (c-a) $\text{CuFeMnO}_4(\text{PT})/\text{CuCr}_2\text{O}_4(\text{DB})$, and (c-b) lab-coated Pyromark.

detail in future research, as the reflectance behavior in near-IR spectrum above 1 μm differs from the results of isothermal tests observed in Fig. 7(a). Compared to the lab-coated Pyromark sample which has FOM of 0.8968 after 1 cycle and FOM endurance of 0.9987 after 100 cycles

calculated by Eq. (3), $\text{CuFeMnO}_4(\text{PT})/\text{CuCr}_2\text{O}_4(\text{DB})$ sample reaches the higher FOM of 0.902 and better FOM endurance of 0.9993 after 100 cycles. As shown in Fig. 7(c), the tandem-structured sample kept the black surface color by high light absorption after the 100-cycle annealing, whereas the lab-coated Pyromark sample turned brownish after 1 cycle and 100 cycles because of the higher reflectance at wavelength above 600 nm. Fig. 8(b-1) and (b-2) show that the porous surface morphology of CuFeMnO_4 layer coated on the dense CuCr_2O_4 layer is preserved to be almost indistinguishable to 1-cycled samples in micro-scaled image after the thermal cycling tests. Nano-scaled morphology change needs to be studied in future research to analyze the effect of morphology change on reflectance through thermal tests. When evaluating the porous structure based on these SEM images, lab-coated Pyromark sample has a much denser surface structure than $\text{CuFeMnO}_4(\text{PT})/\text{CuCr}_2\text{O}_4(\text{DB})$ samples, as compared in Fig. 8. Lab-coated Pyromark sample contains only very small nanopores on surface which cannot decrease reflectance in a wide spectral range including visible and near-IR. Furthermore, the porous surface structure of our tandem layers is more effective to accommodate volume change during a rapid temperature change, which can prevent micro-cracks and delamination after many thermal cycles.

For high temperature application in air, there could be a concern of oxidation of the substrate (Inconel) and/or element diffusion between the black oxide and the Inconel. The preserved high FOM and no sign of delamination after thermal cycling (100 cycles) and thermal annealing (500 h at 750 °C) suggest that the Inconel is stable within the experimental conditions tested in this study. It is known that Inconel 625 can form a protective layer upon oxidation, which prevents further damage to the material (Lefebvre et al., 2008). It has been shown that Inconel 625 is stable in environments less than 900 °C and spinel oxide coatings (such as CuCr_2O_4) can be used to block diffusion and oxidation of Cr (in the Inconel substrate) (Wang, 2013). Therefore, we believe Inconel 625 to be a suitable substrate for our high temperature application at 750 °C. However, testing for a period substantially longer than 500 h needs to be carried out in order to fully evaluate its suitability for ~ 30 -year service in future high-temperature CSP plants.

The lack of delamination suggests that the coefficient of thermal expansion (CTE) mismatch between the top and bottom layer is important. CTE of the substrate is about 16 ppm/K between 25 °C and 800 °C (Haynes data sheet). The coating is made of spinel oxides plus a very small amount of spin-on glass (methyl phenyl polysiloxane). The spinel oxides have CTE values ranging from 7 to 12 ppm/K (Petric and Ling, 2007) and the spin-on glass generally has a high CTE greater than 12 ppm/K (Oh and Ree, 2004), so the CTE of the coating will be slightly higher than 7–12 ppm/K. However, the coating has a porous structure (even in the ‘dense’ layers, as shown in Fig. 6),

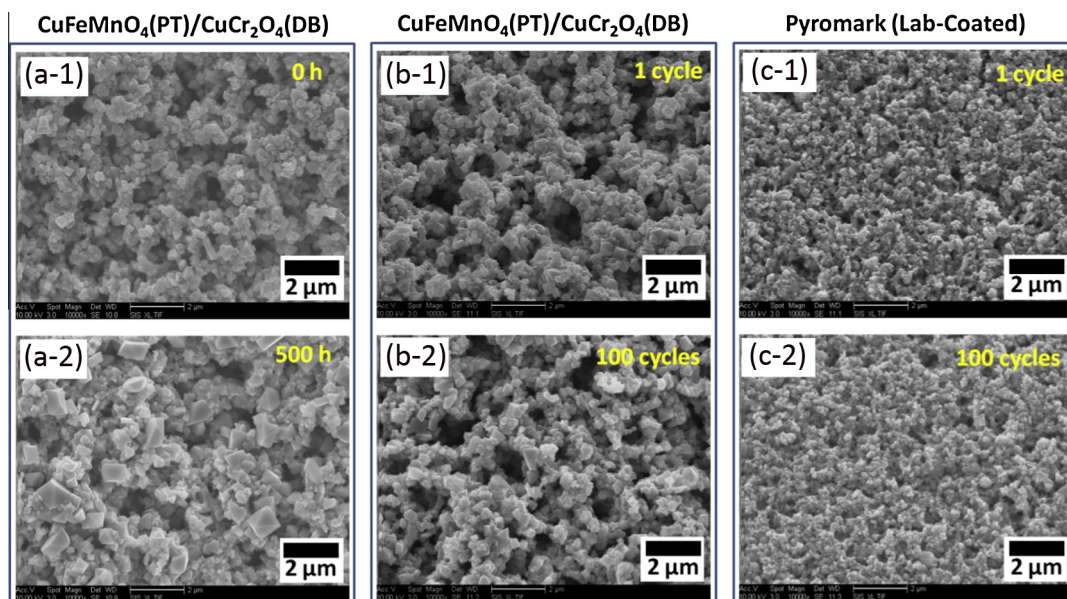


Fig. 8. SEM images of surface morphologies obtained from isothermal tests at 750 °C for 500 h in air for CuFeMnO₄(PT)/CuCr₂O₄(DB) solar absorbing samples ((a-1) and (a-2)), and the morphologies from the rapid thermal cycling tests (RT-750 °C) for CuFeMnO₄(PT)/CuCr₂O₄(DB) samples ((b-1) and (b-2)) and lab-coated Pyromark samples ((c-1) and (c-2)).

so it can accommodate thermal stress caused by the potential CTE mismatch. We believe this could be an important reason for the excellent adhesion shown in our samples.

4. Conclusion

Two types of black oxide nanoparticles were synthesized including Cu–Fe–Mn oxides and Cu–Cr oxides, and their compositions and crystallization conditions were optimized based on the reflectance data and FOM evaluations. Utilizing these nanoparticles, 2-layered tandem structure of solar absorbing layer was devised with a porous CuFeMnO₄ top layer and a dense CuCr₂O₄ bottom layer. These layers were chosen to have complementary absorption in the visible and infrared regions. The tandem structure showed an excellent FOM value (0.903), indicating 90.3% solar to thermal conversion efficiency. This exceeds that of an solar absorbing layer made with a commercial Pyromark black paint. From FOM thermal endurance tests, 2-layered CuFeMnO₄(PT)/CuCr₂O₄(DB) solar absorbing sample shows FOM endurance above 0.99 after 750 °C/500 h in air. This tandem-structured solar absorbing layer with excellent FOMs and thermal endurance can be used for the cost-competitive next generation concentrating solar power plants.

Acknowledgement

The support of this research by Department of Energy through DOE SunShot Project (DE-EE0005802) is acknowledged.

Appendix A. Supplementary material

Supplementary data associated with this article can be found, in the online version, at <http://dx.doi.org/10.1016/j.solener.2016.03.007>.

References

- Ambrosini, A., Lambert, T.N., Bencomo, M., Hall, A., vanEvery, K., Siegel, N.P., Ho, C.K., 2011. In: Proceedings of the ASME 2011 5th International Conference on Energy Sustainability, ES2011-54241.
- Bayon, R., San Vicente, G., Maffiotte, C., Morales, A., 2008. *Renewable Energy* 33 (2), 348–353.
- Behar, O., Khellaf, A., Mohammedi, K., 2013. *Renew. Sustain. Energy Rev.* 23, 12–39.
- Burhardt III, J.J., Heath, G.A., Turchi, C.S., 2011. *Environ. Sci. Technol.* 45, 2457–2464.
- Chukalkin, Y.G., Petrov, V.V., Shtirs, V.R., Goshchitskii, B., 1985. *Phys. Status Solidi A* 92, 347–354.
- Crottaz, O., Kubel, F., Schmid, H., 1997. *J. Mater. Chem.* 7, 143–146.
- Hayman, B., Wedel-Heinen, J., Brøndsted, P., 2008. *MRS Bull.* 33, 343–353.
- Haynes data sheet, retrieved from <<https://www.haynesintl.com/pdf/h3073.pdf>>.
- Ho, C.K., Iverson, B.D., 2014. *Renew. Sustain. Energy Rev.* 29, 835–846.
- Ho, C.K., Mahoney, A.R., Ambrosini, A., Bencomo, M., Hall, A., Lambert, T.N., 2014. *J. Solar Energy Eng.* 136, 014502-1–014502-4.
- Jogalekar, S., 1967. *Indian J. Pure Appl. Phys.* 5, 9–13.
- Kargar, A., Yavuz, S., Kim, T.K., Liu, C.H., Kuru, C., Rustomji, C.S., Jin, S., Bandaru, P.R., 2015. *Appl. Mater. Interfaces* 7, 17851–17856.
- Kelzenberg, M.D., Boettcher, S.W., Petykiewicz, J.A., Turner-Evans, D. B., Putnam, M.C., Warren, E.L., Spurgeon, J.M., Briggs, R.M., Lewis, N.S., Atwater, H.A., 2010. *Nat. Mater.* 9, 239–244.
- Kennedy, C.E., 2002. Review of Mid- to High-Temperature Solar Selective Absorber Materials, NREL/TP-520-31267.
- Khamwannah, J., Zhang, Y., Noh, S.Y., Kim, H., Frandsen, C., Kong, S. D., Jin, S., 2012. *Nano Energy* 1, 411–417.

- Kocsis, V., Bordács, S., Varjas, D., Penc, K., Abouelsayed, A., Kuntscher, C.A., Ohgushi, K., Tokura, Y., Kézsmárki, I., 2013. *Phys. Rev. B* 87, 064416.
- Lefebvre, L.-P., Banhart, J., Dunand, D.C., 2008. *Adv. Eng. Mater.* 10, 775–787.
- Levelized Cost and Levelized Avoided Cost of New Generation Resources, 2014. Annual Energy Outlook 2014, US Energy Information Administration (EIA), DOE/EIA-0383ER.
- Levinson, R., Berdahl, P., Akbari, H., 2005. *Sol. Energy Mater. Sol. Cells* 89, 351–389.
- Liang, J., Peng, Q., Wang, X., Xhang, Z., Wang, R., Qiu, X., Nan, C., Li, Y., 2005. *Inorg. Chem.* 44, 9405–9415.
- Moon, J., Lu, D., VanSaders, B., Kim, T.K., Kong, S.D., Jin, S., Chen, R., Liu, Z., 2014. *Nano Energy* 8, 238–246.
- Moon, J., Kim, T.K., VanSaders, B., Choi, C., Liu, Z., Jin, S., Chen, R., 2015. *Sol. Energy Mater. Sol. Cells* 134, 417–424.
- Oh, W., Ree, M., 2004. *Langmuir* 20, 6932–6939.
- Peng, K., Xu, Y., Wu, Y., Yan, Y., Lee, S.-T., Zhu, J., 2005. *Small* 1, 1062–1067.
- Petric, A., Ling, H., 2007. *J. Am. Ceram. Soc.* 90, 1515–1520.
- Tackling Challenges in Solar, 2014 SunShot Initiative Portfolio, US Department of Energy, DOE/EE-1081.
- Tsakalacos, L., Balch, J., Fronheiser, J., Korevaar, B.A., Sulima, O., Rand, J., 2007. *Appl. Phys. Lett.* 91, 233117-1–233117-3.
- Turner, J.A., 1999. *Science* 285, 687–689.
- Varun, Bhat, I.K., Prakash, R., 2009. *Renew. Sustainable Energy Rev.* 13, 1067–1073.
- Vince, J., Šurca Vuk, A., Opara Krašovec, U., Orel, B., Köhl, M., Heck, M., 2003. *Sol. Energy Mater. Sol. Cells* 79, 313–330.
- Wang, Y., 2013. Structure and Electrical Conductivity of Mn-based Spinel Used as Solid Oxide Fuel Cell Interconnect Coatings (Master's thesis).
- Yuan, W., Liu, X., Li, L., 2014. *Appl. Surf. Sci.* 319, 350–357.
- Zhu, J., Cui, Y., 2010. *Nat. Mater.* 9, 183–184.